Materials Science & Engineering A 955 (2026) 149867

Contents lists available at ScienceDirect

Materials Science & Engineering A

journal homepage: www.elsevier.com/locate/msea

Mitigating the challenges in additive manufacturing of refractory complex concentrated alloys using Ti alloying via multi-material feedstock approach

Magesh Kumaravel [a], Joachim Gussone [b], Meaghi Sikder [a], Amir Ardeshiri Lordejani [a], Ida S. Berglund [c], Jan Haubrich [b], Sara Bagherifard [a], Mario Guagliano [a,*]

[a] *Politecnico di Milano, Department of Mechanical Engineering, Via La masa 1, 20158, Milan, Italy*
[b] *German Aerospace Center, Institute for Frontier Materials on Earth and in Space, Linder Hohe, D-51147, Cologne, Germany*
[c] *Thermo-Calc Solutions AB, Solna, Sweden*

ARTICLE INFO

Keywords:
Multi material additive manufacturing
Mixed feedstock
Refractory complex concentrated alloy
High entropy alloy

ABSTRACT

The development of novel refractory complex concentrated alloy material systems for extreme environments, despite the promise, is hindered by significant processing challenges during fabrication. These challenges primarily stem from their intrinsic properties: high hardness and brittle nature restrict deposition through impact-based approaches such as cold spray additive manufacturing (CSAM), while the wide variation in melting temperatures among constituent elements limits the processability by melting and solidification - based additive manufacturing techniques such as laser-based powder bed fusion (LB-PBF). In this study, a composite feedstock approach was employed to mitigate the aforementioned-challenges during CSAM and LB-PBF processing. Commercially pure Ti was employed as the secondary material and was mixed with a custom-developed TaNbTiVCr alloy at varying volumetric ratios. The CSAM and LB-PBF printed specimens were systematically characterized in terms of their microstructure and microhardness. CSAM and LB-PBF printed specimens with different volume fractions of mixing demonstrated excellent build quality, with negligible porosity and crack formations, albeit with inhomogeneous microstructures. In the case of CSAM, the specimen with highest TaNbTiVCr content retained comparable hardness to that of the feedstock powder, despite Ti addition. The Ti particles offered a cushioning effect to the impacting TaNbTiVCr particles, thereby limiting the inter-particle interaction between them, aiding the deposit build-up. On the other hand, Ti addition for the LB-PBF processing played a critical role in inhibiting the formation of hot-cracks and lack-of-fusion porosities. However, this was at an expense of lower hardness compared to the CSAM counterparts. Overall, this systematic study highlights the potential of employing a composite feedstock approach to significantly enhance the processability of the complex refractory alloys through additive manufacturing.

Nomenclature:

AM	Additive manufacturing
BCC	Body centered cubic
BSE	Back scattered electron
CCA	Complex concentrated alloy
CSAM	Cold spray additive manufacturing
EDS	Energy dispersive X-ray spectroscopy
EIGA	Electrode induction melting inert gas atomization
FCC	Face centered cubic
HEA	High entropy alloy
LB-PBF	Laser-based powder bed fusion
OM	Optical microscopy
RCCA	Refractory complex concentrated alloy
XRD	X-ray diffraction
SEM	Scanning electron microscopy
VED	Volumetric energy density

1. Introduction

Complex concentrated alloys (CCA) are created by combining higher concentrations (5–35 %) of different principal elements and have been identified to offer superior properties when compared to alloys prepared

---

* Corresponding author.
E-mail address: mario.guagliano@polimi.it (M. Guagliano).

https://doi.org/10.1016/j.msea.2026.149867
Received 12 November 2025; Received in revised form 19 January 2026; Accepted 29 January 2026

by conventional alloying processes. The inherent core-strengthening effects of these alloys results in superior properties. These strengthening mechanisms include lattice distortions due to the mismatch of atomic radii, the high configurational entropy effect (solid solution strengthening), and the cocktail effect (ability to manifest properties different from those of different constituent elements) [1–3].

Despite the ongoing research and the new developments in the field of CCAs including high entropy alloys (HEA) from the point of view of alloy composition, the venture into the refractory CCAs is still quite novel [4]. These alloys are made of refractory metal elements from the periodic table as their principal elements, adding a few other elements like Al or Si, for improved properties [1], even in comparison with Ni-based superalloys and Nb-based C103. As these alloys have advanced, significant work has focused on assessing appropriate manufacturing technologies for them [5–7].

Additive manufacturing (AM) of these RCCA poses a significant challenge since the melting temperatures of the elements present in these alloys are considerably higher and comprise a broader range [8]. Apart from these complex alloys, there exist challenges to process high-melting point refractory metals even in its pure form. For instance, pure W produced by laser-based powder bed fusion (LB-PBF) is reported to typically develop microcracks due to steep thermal gradients and W's high ductile-brittle transition temperature [9,10]. Hence, these factors play a critical role in processing the complex alloys made solely from refractory materials.

Besides the melting-solidification based AM techniques such as LB-PBF, also solid-state cold spray additive manufacturing (CSAM) has shown limitations in processing these alloys [11]. Having reported the limitations in producing high-quality pre-alloyed feedstock, in our previous study we reported the major challenges associated with the AM of the pre-alloyed 7 element complex concentrated alloy TaNbWTiVMoCr. LB-PBF processing resulted in a large network of microcracks, exhibiting poor build quality. In addition to these challenges, the vast differences in melting temperatures among the constituent elements in the mix resulted in higher crack densities of up to 9 mm/mm^2. Heating the build plate to 1000 °C reduced crack density to 1 mm/mm^2 but did not eliminate them entirely. Homogenous microstructures, along with uniformity in chemical concentrations and purity in terms of interstitial contents (O_2 and N_2), proved to be critical for its processability. The latter was shown to have an effect on the strength-ductility relationships of the alloy at lower temperatures. On the other hand, CSAM processing of this alloy resulted in little to no deposit formation [11].

In CSAM, mixing a suitable secondary material that exhibits good ductility with these complex alloys can be a promising strategy to overcome these challenges. Recently, CSAM has been employed to produce deposits consisting of multi-metallic or mixed feedstocks in several studies [12–14]. These studies have often been performed with the view of leveraging the merits of the required properties that the constituent materials offer for respective applications. In the domain of CCAs, FeCoNiCrMn was sprayed with alumina as a reinforcement material to enhance the wear resistance of the deposit. Results showed that the composite deposits showed better sliding wear performance, compared to the pure FeCoNiCrMn deposit. However, the deposits revealed the presence of large interparticle gaps at the interfaces between the two materials [15]. A similar face centered cubic (FCC) based CoCrFeNi alloy was added to an Al matrix and the deposit was friction stir processed to improve the deposit characteristics. Unlike the ceramic/cermet composites, this study revealed the presence of a 0.5 μm thick diffusion layer at the interface between Al and CoCrFeNi particles, in the as-sprayed condition, which was further enhanced to 1 μm by friction stir processing [16]. The same HEA, mixed with a small atomic percentage of Ti resulted in mechanical interlocking of the deposits without any diffusion layers detected in the as-sprayed state. However, diffusions zones were observed when the deposits were heat treated up to at least 800 °C. Higher hardness of the Ti counterpart in the feedstock mix, was also reported to enhance the densification of the deposits in comparison with the as-sprayed pure CoCrFeNi [17].

With regard to LB-PBF processing, the motivation for employing premixed feedstock stems from the possibility of opening up a new route for alloy design. Addition of 10 wt% Mo to Ti6Al4V resulted in improved strength and ductility [18]. In another study, the addition of 25 % wt Ta to CP Ti was observed to increase the strength-modulus ratio and fatigue life, compared to LB-PBF CP Ti [19,20]. Despite this possibility, challenges associated with chemical heterogeneity and formation of intermetallic phases still exist [21]. The broader melting/freezing temperature range comes into effect especially for LB-PBF processing. The mixed feedstock resulted in an inhomogeneous microstructure when 35 wt% Nb was added to Ti owing to insufficient melting. However, despite the fact that the pre-alloyed Ti35Nb exhibited passivation due to a stable oxide layer, both pre-alloyed and mixed feedstock resulted in similar electrochemical corrosion behaviors [22]. Wang et al. reported the obvious challenges of chemical heterogeneity in the same mixture [23], reinstating the significance of parametric optimizations especially for these mixed feedstocks. In-situ alloying of refractory elements such as W, Mo, Ta, Nb, V demonstrated the retention of unmolten W particles [24].

Ti is a relatively ductile refractory metal and its addition to refractory type CCAs is expected to improve the ductility and toughness of manufactured components. Xu et al. added Ti to the refractory CCA feedstock NbMoTaW to address its low room-temperature ductility, caused by oxygen entrapment in the grain boundaries during solidification. The Ti addition resulted in no change to the primary phase, which remained single phase body centered cubic (BCC). The presence of Ti also lowered the oxygen enrichment at grain boundaries by forming TiO_2. These TiO_2 precipitates contributed to dispersion strengthening, enabling the mixed feedstock specimens to achieve a yield strength of about 22 % higher than that of Ti free NbMoTaW [25]. Addition of Ti to alloys such as NbMoTaW and VNbMoTaW was shown to enhance the room temperature strength and ductility. TiNbMoTaW and TiVNbMoTaW showed 27 % and 21.5 % increase in yield strength at 25 °C. The study also demonstrates an enhancement of yield strengths even at elevated temperatures up to 1200 °C [26]. The possibility of using a mixed material feedstock with CSAM and LB-PBF, as discussed above, also presents opportunities for the development of functionally graded materials. Such components manufactured can be particularly advantageous in applications where the service conditions vary across different regions or geometries of the part, demanding location-specific material properties [27–29].

In this study we assess the manufacturability of refractory complex concentrated alloys using two distinct manufacturing techniques: CSAM and LB-PBF with pre-mixed powder. A five-element, non-equiatomic refractory CCA (TaNbTiVCr; RCCA) was considered by incorporating commercially pure Ti (CP-Ti, Grade 1) powder at varying volume percentages, to optimize the final feedstock composition with maximum RCCA retention. This customized RCCA feedstock was expected to have better ductility compared to the previously reported TaNbWTiVMoCr [11], due to modifications in the chemical compositions to improve the tolerance towards oxygen uptake and particle deformability. However, the powder showed similar microstructural features to the one reported in Ref. [11] (elaborated in coming sections) that were found to be very critical for CSAM and LB-PBF processing in the previous work, further highlighting the challenges associated with RCCA feedstock production. The existing cold spray studies on mixed feedstocks often involve CCAs that are primarily FCC based, focusing on improving on the deposits' mechanical responses. On the other hand, in the case of LB-PBF, the above discussed studies provide a valuable insight with regards to the benefits on Ti addition to refractory type-CCAs. Hence, this study focused on the possibility of enhancing buildability through using mixed feedstock powders using two distinct AM technologies of CSAM and LB-PBF for processing (RCCA + Ti), critically analyzing the results in terms of general and specific build quality indexes, microstructure and microhardness, which can help in understanding the fundamental mechanical behavior.

2. Materials and experimental methods

The RCCA TaNbTiVCr powder, hereafter referred to as “RCCA” only, was custom designed by Thermo-Calc solutions AB (Sweden) and subsequently manufactured by TaNiobis GmbH (Germany) through Electrode Induction Melting Inert Gas Atomization (EIGA). The D10, D50 and D90 values representing their particle size distribution are 15.72 μm, 31.44 μm and 67.26 μm respectively. Two batches of CP-Ti, Grade 1 were used, both manufactured via gas atomization, with sizes +15/-45 μm and +20/-63 μm for CSAM processing and LB-PBF processing respectively. Scanning electron microscopic (SEM) images of the surface morphology of the feedstock powders are shown in Fig. 1a and c.

The powder particles were embedded in conductive polymeric resin and subsequently polished to observe their cross-sectional morphologies. The cross-section of the RCCA particles revealed the presence of isolated islands (Fig. 1b), which were enriched with Tantalum (Ta) and Niobium (Nb) in some instances as evidenced by energy dispersive X-ray Spectroscopy (EDS) (Fig. 2a). This heterogeneity may have stemmed from the significant differences in freezing ranges between Ta/Nb and other elements within the RCCA [11]. X-ray diffraction (XRD) analysis further indicated that the RCCA powder was composed of a single-phase body-centered cubic (BCC) structure (Fig. 2b). The broad asymmetric reflections can also be explained by the chemical heterogeneity of the RCCA powder. CP-Ti, on the other hand, exhibited a single-phase hexagonal close-packed structure. The cross-sectional image of a single CP-Ti particle is shown in Fig. 1d.

2.1. Cold spray deposition

CSAM deposits were fabricated at Politecnico Milano, using the Impact Innovations 5/11 system, which employed nitrogen as the working gas and utilized two powder feeders capable of *in-situ* powder mixing. The spray parameters were optimized specifically for the ductile component of the composite feedstock, that is, CP-Ti. The parameters resulting from this optimization are listed in Table 1.

In order to evaluate the optimum ratio of mixing, for maximum RCCA retention, 3 feedstock compositions were selected for spraying: Ti + 20 vol% RCCA (RCCA-20), Ti + 50 vol% RCCA (RCCA-50), and Ti + 80 vol% RCCA (RCCA-80). The Ti and RCCA powders were introduced through separate powder feeders and mixed *in situ* during spraying by adjusting the powder feed rates to achieve the desired volume fractions, as outlined in Table 2. The aluminum alloy 6082 T6 was selected as the substrate material.

The deposits were sectioned and embedded in a conductive polymeric resin. Subsequently, the specimens were ground and polished for cross-sectional characterization. Optical microscopy (OM) and SEM were used to examine the cross-sections to assess the deposit thickness, retained RCCA content, porosity, particle flattening ratios, and deposition efficiency. Global porosities were measured using low magnification micrographs from OM stitched together, whereas the local porosities were measured using high magnification back scattered electron (BSE) images from SEM. The flattening ratios of the particles were calculated by the ratio of the diameters of circles circumscribing to those inscribing the splats (Fig. 3). At least 30 deformed particles were considered in the measurements. The overall deposition efficiency of the deposits was determined by the ratio of the weight of the specimen after deposition to the substrate weight before deposition. To specifically estimate the deposition efficiency of RCCA, the retained RCCA content in each volumetric composition was considered as the retained RCCA volume percentage, assuming the deposit geometry to be a perfect cuboid.

2.2. Laser-based powder bed fusion

LB-PBF-printed specimens were fabricated using an SLM Solutions 280HL machine equipped with a 400 W ytterbium fiber laser (IPG, model YLR-400-WC) with a wavelength of 1071 nm, operating in continuous wave-mode with a Gaussian beam shape at the German Aerospace Centre, Cologne, Germany. The laser spot size was ca. 80 μm. The scanning strategy adopted was chess pattern with sizes 5 mm × 5 mm. High-purity argon was continuously supplied to the building chamber. The LB-PBF setup was also modified with a gas purification system similar to that of a glove box (mBraun UNILab LMF) to reduce oxygen levels even further during processing (to <10 ppm, i.e. below the real detection limit of λ-sensors, but still observable with quadrupole mass spectroscopy in the process atmosphere) the and also capture possible residual humidity if introduced through the Argon gas.

As the material combinations under study (RCCA and Ti mixture) are

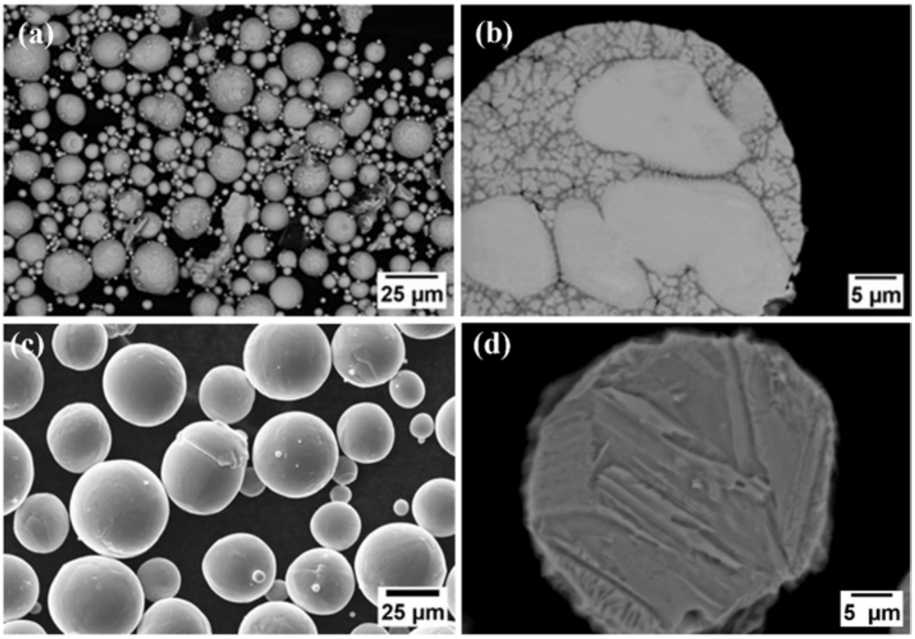

Fig. 1. Morphology and cross-sectional SEM micrographs of (a, b) RCCA, (c, d) pure Ti (+15/-45 μm) feedstocks respectively.

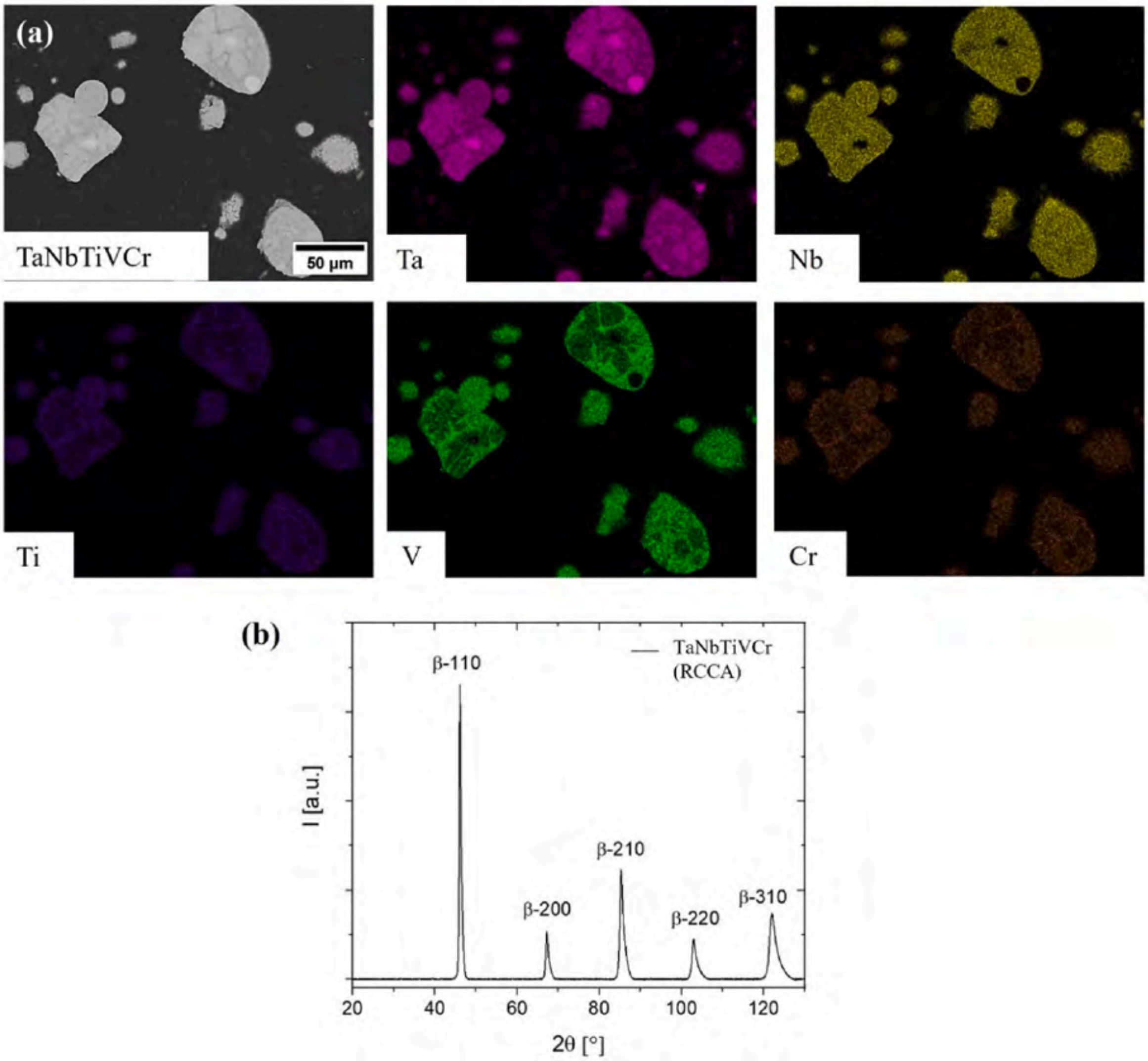

Fig. 2. (a) EDS mapping of the chemical composition of RCCA powder (b) XRD diffractogram indicating the presence of single-phase BCC.

Table 1
CSAM process parameters.

Parameters	
Gas stagnation pressure (bar)	35
Gas stagnation temperature (°C)	800
Nozzle transverse speed (mm/s)	250
Powder feed rate (rpm)	2.0
Step size (mm)	1
Stand-off distance (mm)	40

Table 2
Volume fraction of RCCA and equivalent CS feed rates.

Volume fraction of RCCA in feedstock	CS specimen nomination	Ti + RCCA	
		RCCA feed (rpm)	Ti feed (rpm)
20 %	RCCA-20	0.4	1.6
50 %	RCCA-50	1	1
80 %	RCCA-80	1.6	0.4

fairly novel, parametrical optimizations were performed on a larger scale with a full factorial design of experiments involving variations in the two main process parameters associated with LB-PBF (Table 3). The resulting volumetric energy densities (VED) varied between 80 and 266.67 J/mm^3. For these trials, CP-Ti (+20/-63 µm) and RCCA powders were pre-mixed in an argon atmosphere. The volume fractions of mixing were chosen to replicate the retained RCCA volume observed in the CSAM deposits, thereby facilitating a direct comparison between the 2 a.m. techniques. In all cases, the specimens were built on Ti6Al4V plates of 50 × 50 × 10 mm^3, without base plate pre-heating, and the specimen sizes were 5 × 5 × 10 mm^3.

The LB-PBF specimens were prepared for characterization following the same procedure as outlined for the preparation of the CSAM specimens, and similar microscopic observations were performed. After a rigorous process parameter optimization, specimens with best characteristics and optimized process parameters from those listed in Table 3 were selected for each volumetric composition for in-depth hardness evolution analyses. Vickers microhardness measurements were performed along the build direction for both the CSAM and LB-PBF specimens. Indentations were done using a 300 g load and a dwell time of 15 s per specimen, with at least three measurements at each height along the build direction.

Additionally, to evaluate the effect of Ti additions, both AM techniques were employed to manufacture RCCA specimens without Ti content. The parameters chosen were similar to the range reported in Ref. [11]. For CSAM, the gas pressure and gas temperature were 50 bar and 800 °C, respectively. The trials were performed on Al alloy substrate

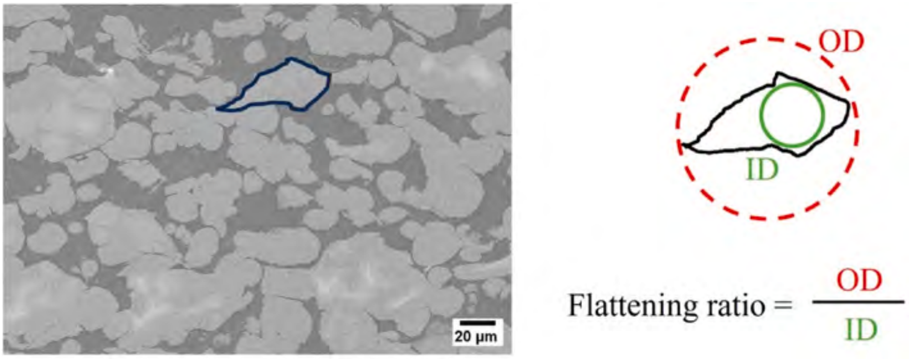

Fig. 3. Calculation of flattening ratios using BSE - SEM images.

Table 3
LB-PBF process parameters.

Parameters	
Laser power (W)	180
Scan speed (mm/s)	450, 600, 750
Hatch spacing (μm)	50,100
Layer thickness (μm)	30

for direct comparisons. For LB-PBF, the specimens were printed using 250 W laser power, 600 mm/s scan speed, 100 μm hatch spacing and 30 μm layer thickness. The base plate used was made of Ti6Al4V with no pre-heating.

3. Results

3.1. Cold spray

3.1.1. Build quality and microstructural analysis

A detailed examination of the composite deposits produced via CSAM revealed that increasing the volume fraction of RCCA in the feedstock correspondingly reduced the overall thickness of the resulting deposits. Furthermore, the proportion of RCCA retained within the final deposit consistently rose as the RCCA content in the feedstock increased (see Fig. 4a–c & 4d-f). For instance, Fig. 4g shows that the RCCA-20 deposit (23 % RCCA retained) exhibited a thickness of approximately 3.15 mm, whereas the RCCA-80 deposit (61 % RCCA retained) yielded a reduced thickness of 1.3 mm.

As expected, the overall deposition efficiency decreased as the RCCA content in the feedstock increased (Fig. 5a). The maximum overall deposition efficiency was 97.4 % for the RCCA-20 deposit, whereas the RCCA-80 deposit exhibited a significantly lower efficiency of 32.9 %. This reduction in the overall deposition and the deposit thickness with increase in RCCA content can be attributed to the poor deposition efficiency of RCCA feedstock due to its inherently superior hardness, and thus brittle nature [11]. The specific deposition efficiency of RCCA decreased with increasing RCCA content in the deposit. However, a notable improvement in terms of deposition efficiency of RCCA is seen with respect to the previous trials conducted with a similar RCCA TaNbWTiVMoCr [11], where minimum to no deposition was observed irrespective of the substrate material used. In contrast, in the current study, the addition of a mere 20 % volume fraction of Ti to the feedstock resulted in raising the specific RCCA deposition efficiency from almost none to 47.6 %.

Addition of ductile Ti particles facilitates the retention of brittle RCCA within the deposit by absorbing impact energy, thereby mitigating the risk of RCCA fracture, which was observed earlier in Ref. [11]. Microscopic images shown in Fig. 4d–f indicate that the particle-particle interface between Ti and RCCA is distinct, suggesting that the inter-particle bonding is primarily due to mechanical interlocking rather than metallurgical bonding. Overall, the cross-sectional analysis of the deposits exhibited an almost uniform distribution of the feedstock powders.

The flattening ratio of splats in CSAM deposition is crucial in determining deposit quality and properties, [30–32], as it can be correlated to increased grain recrystallization [33], and inter-splat bonding [34]. Analyzing flattening ratio of the RCCA particles in these deposits indicated increase with the retained RCCA content in the deposit (Fig. 5b). This could be the result of the enhanced peening effect associated with the higher volume of RCCA in the sprayed feedstock. The higher magnitude of the flattening ratios suggests that the particles were ductile enough to absorb the impact energy, facilitated by an adequate volume of ductile Ti retained in the deposit. RCCA particles in the RCCA-80 deposit exhibited a flattening ratio of 1.97, compared to 1.37 for those in the RCCA-20 deposit.

The local porosity measured using micrographs captured by SEM at 2000 × (Fig. 6a) in all cases was significantly lower than the corresponding global porosity, measured with an OM (Fig. 6b), although both showed similar trends (Fig. 5c). Globally, the porosity ranged from 3.6 % for RCCA-80 to a peak value of 7.9 % for RCCA-50, with the RCCA-20 deposit showing 4.3 %. As the volume of RCCA fraction in the deposit increased, porosity initially became more pronounced, likely due to the "shadow effect" wherein inherent hardness of RCCA particles limited their deformation and prevented the ductile Ti particles from filling the pores. However, with a further increase in the RCCA content, as observed in the case of RCCA-80, the porosity decreased to its lowest value. This can be attributed to the more pronounced peening effect reflected also in the flattening of the RCCA particles in the case of RCCA-80.

3.1.2. Microhardness measurements

The average microhardness of the deposits increased with the retention of the RCCA content. RCCA-20, -50, and −80 deposits demonstrated microhardness values of 238.58 HV, 339.06 HV and 410.39 HV, respectively (Fig. 7a). CSAM pure Ti with similar deposition parameters is reported to yield deposits with microhardness ranging from 187 HV to 243 HV [35–37]. Notably, the microhardness of the RCCA-20 deposit, with a lower retained RCCA content, was at the higher end of this range. Furthermore, the RCCA-80 deposit, which retained 61 % RCCA, exhibited a microhardness value comparable to that of the RCCA feedstock, measured on particle cross sections to be 479 ± 45 $HV_{0.025}$. This indicates that, despite the presence of nearly 40 % volume fraction of ductile Ti particles in the deposit, the hardness was not significantly compromised. The inherent effect of work hardening induced during the CSAM process may have contributed to the enhanced hardness of the Ti and RCCA particles. It should also be noted that the amount of RCCA particles retained in the deposits might have had an added effect on the work hardening of the particles (evident from the flattening ratios), leading to a higher overall hardness of the deposit.

An in-depth investigation of the variation in microhardness along the

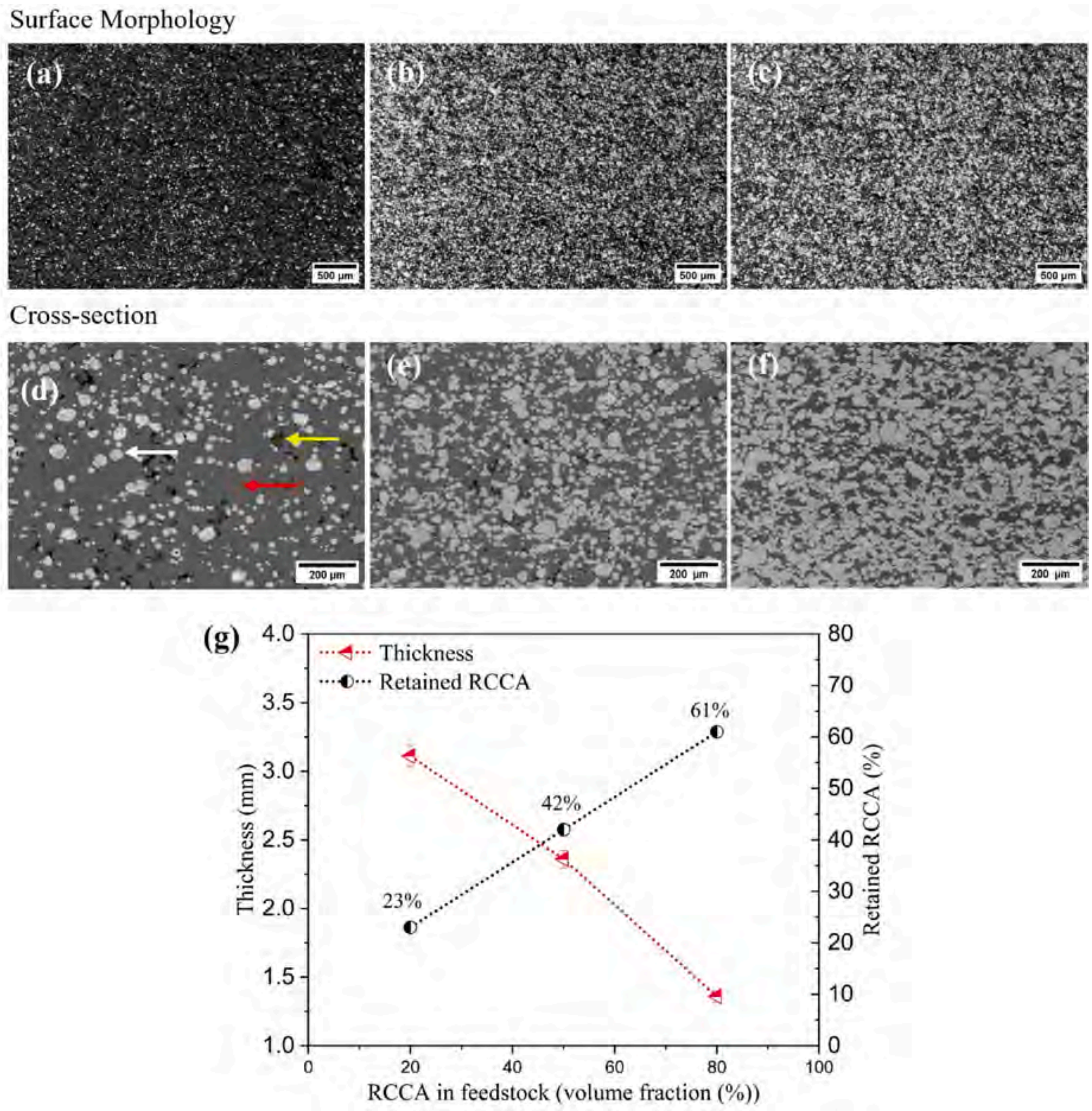

Fig. 4. SEM Back scattered electron micrographs of surface morphology, cross-section of (a, d) RCCA-20, (b, e) RCCA-50, (c, f) RCCA-80; (white, red and yellow arrows indicate RCCA, CP-Ti and porosity respectively) (g) Variation of thickness and retained RCCA % in the deposits with respect to the volume fraction of RCCA in the feedstock. (For interpretation of the references to colour in this figure legend, the reader is referred to the Web version of this article.)

build direction (deposit thickness) (Fig. 7b) reveals that the deposits exhibit higher hardness near the interface between the substrate and the deposit. The microhardness gradually decreased towards the top layer. This can be attributed to the heightened peening effect experienced by the initial layers during deposition, leading to excessive plastic deformation and enhanced particle flattening [38]. As the deposition progresses, this effect diminishes towards the outer regions due to a relatively lower number of impacting particles.

3.2. *Laser-based powder bed fusion*

Table 4 presents the selected volume fractions of RCCA incorporated in the LB-PBF builds, which were deliberately chosen to closely correspond with those achieved in the specimens of CSAM experiments. These specimens are denoted as RCCA-60, RCCA-40 and RCCA-25. Fig. 8a presents the morphology of the CP-Ti (grade 1) used for LB-PBF processing. An example of the mixed feedstock (RCCA-40) used for the trials can be referred from Fig. 8b.

3.2.1. *Build quality and microstructural analysis*

Parametrical characterization was performed in terms of the microstructure to assess the build quality. Microscopical analyses revealed that almost all the LB-PBF printed samples were devoid of micro-crack networks, which were prevalent in the case of TaNbWTiVMoCr prints in the previous study [11]. LB-PBF TaNbWTiVMoCr exhibited a crack network of up to 9 mm/mm^2 under similar setup with no base plate heating. Fig. 9 shows the OM images of the cross section of samples with varying volumetric energy densities (VED) (J/mm^3), expressed in equation (1):

$$\mathrm{VED} = \frac{P}{(h * v * t)} \qquad \text{Eq. 1}$$

where P is for the laser power (W), h is the hatch spacing (mm), v is the scan speed (mm/s), and t is the layer thickness (mm).

The densities of all the specimens (measured by image analyses), regardless of volumetric composition, and the operating parameters were measured to be over 99.53 %.

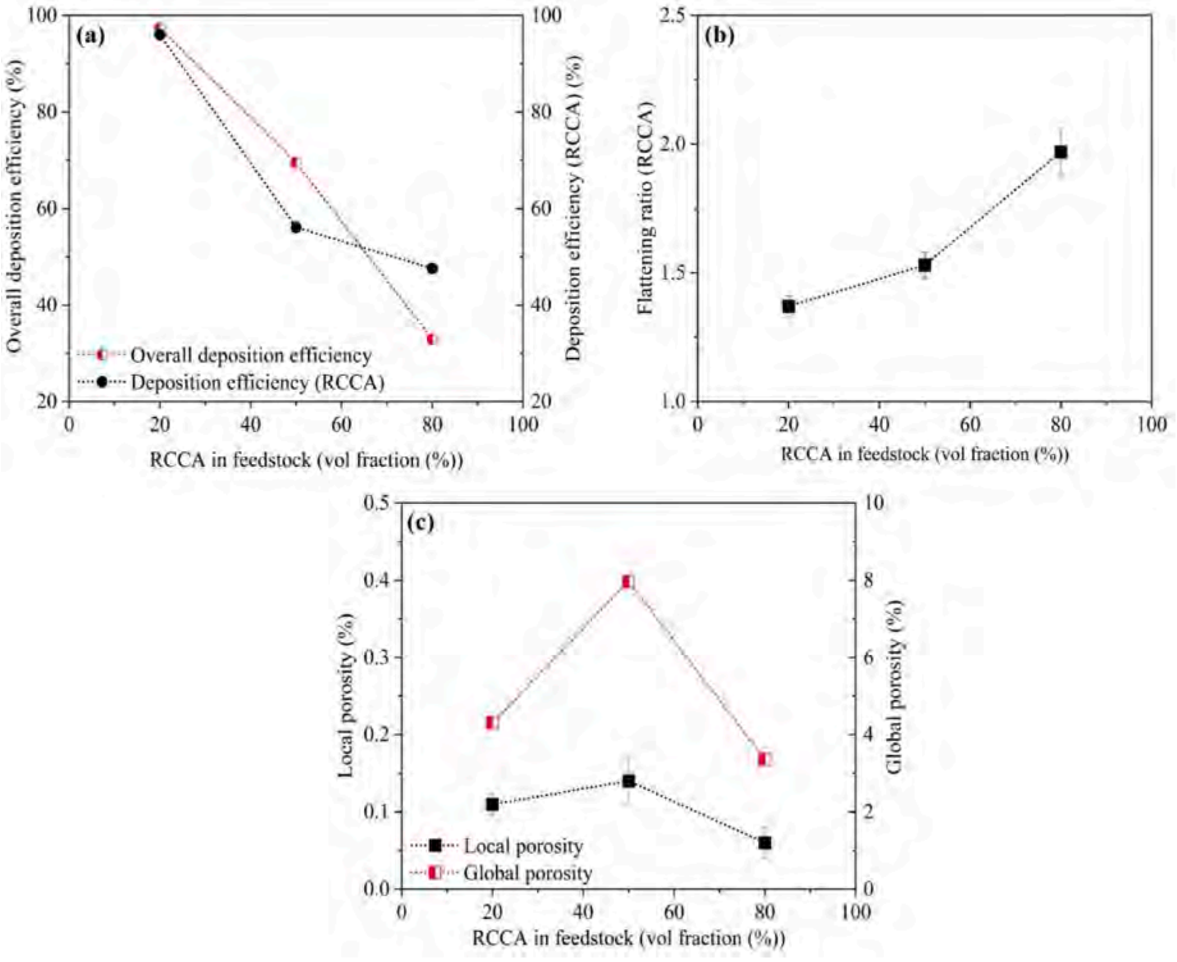

Fig. 5. Variation of (a) deposition efficiency for overall deposit and for RCCA fraction (b) flattening ratios of RCCA in the deposit with increase in RCCA volume fraction in the feedstock (c) local and global porosities.

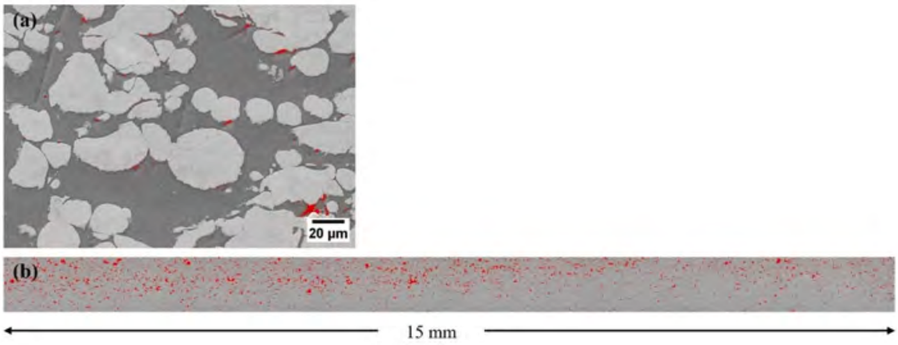

Fig. 6. Red regions indicating (a) Local porosity measured using SEM imaging; (b) Global porosity measured using OM imaging. (For interpretation of the references to colour in this figure legend, the reader is referred to the Web version of this article.)

Fig. 10 illustrates the strong influence of VED during the LB-PBF processing on the microstructure of the printed samples. As expected, the samples printed with lower energy densities exhibited more inhomogeneous microstructures (e.g. Fig. 10a–c & e). This can be attributed to the high melting temperature differences of the constituent materials in the mixture. It should be noted that even at the highest volumetric energy density levels (Fig. 10b–d & f), the microstructure was not entirely homogeneous owing to the much higher melting point of elements present in RCCA, such as Ta and Nb. In fact, unmolten brighter areas were clearly observable in all specimens.

EDS analysis confirmed that these areas were rich in Ta/Nb (Fig. 11), which had the highest melting temperature in the composition of the RCCA. The microstructure also revealed the presence of darker areas that were rich in Ti. The geometry of these dark regions suggests that completely molten Ti tends to fill the voids next to the unmolten RCCA particles, resulting in significantly reduced porosities due to lack of fusion and hot cracks [39,40].

This phenomenon can be well perceived in Fig. 12, illustrating the formation of melt pools in the RCCA-60 specimen built using 266 J/mm^3. Fig. 12a shows the melt pool morphology in the RCCA-60

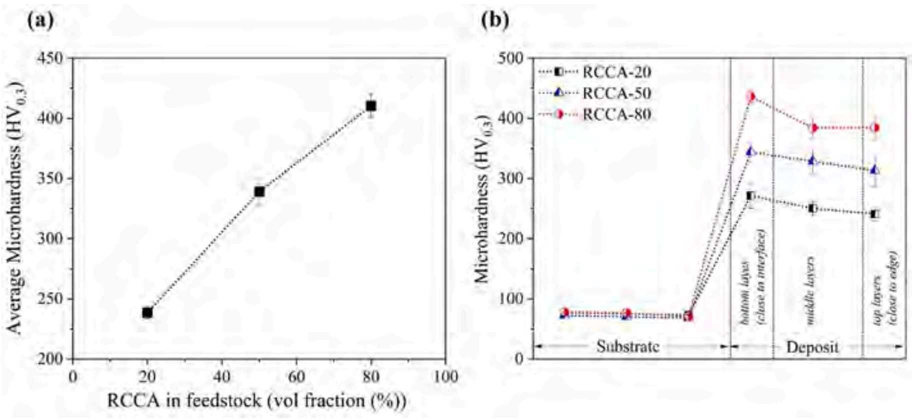

Fig. 7. Microhardness of the CSAM deposits at varying volume fraction of RCCA in the feedstock (a) average microhardness (b) along the thickness of the deposit.

Table 4
Choice of volume fractions of RCCA between CSAM and LB-PBF experiments.

Vol. fraction of RCCA retained in cold spray deposits	Vol. fraction of RCCA in LB-PBF builds	LB-PBF specimen nomination
61 %	60 %	RCCA-60
42 %	40 %	RCCA-40
23 %	25 %	RCCA-25

specimen, revealing the formation of relatively deep melt pools, albeit with the presence of unmolten RCCA particles. Fig. 12b highlights the presence of molten Ti enveloping the unmolten Ta/Nb rich regions, thereby contributing to the improved integrity of built specimens by inhibiting the crack formation.

3.2.2. Microhardness measurements

Fig. 13a illustrates the variation in microhardness along the build direction of LB-PBF specimens fabricated using an energy density of 266.67 J/mm^3. Generally, in LB-PBF, the lower layers display marginally higher hardness compared to the upper layers. This can be attributed to the higher cooling rates experienced at the bottom layers of the specimens, whereas the top layers undergo slower cooling, resulting in the formation of coarser grains [41,42].

On contrary to this phenomenon, RCCA-60 specimens exhibited higher hardness at the top layers, as shown in Fig. 13a. It should be noted that the RCCA-60 specimens were subjected to a few layers of remelting, which is evident from the distinct band observed at the top of the specimen on Fig. 13b. EDS analysis (refer Fig. 14) indicates a significant reduction in Ti content within this region (~10 % compared to an expected 22 %), likely due to evaporation caused by continuous remelting. This zone was also observed to contain higher Ta content (up to 57 % compared to an expected 43 %) and shows a better chemical and microstructural homogeneity. However, this remolten region exhibits several cracks, both in the transverse and longitudinal directions, highlighting the thermal stresses induced by repeated melting cycles and the embrittlement due to the changes in composition.

4. Discussion

Several challenges associated with the processing of the RCCAs with CSAM reported in our previous study [11] includes the critical importance of powder quality, particularly in achieving a homogeneous microstructure and uniformity in chemical concentration. Additionally, these alloys are often characterized by relatively high oxygen content. Despite the slight variation in chemical composition to enhance ductility, the RCCA under study, TaNbTiVCr (Fig. 15b) had similarly high oxygen content, up to 2017 ppm, and exhibited a similar morphology, as TaNbWTiVMoCr, Fig. 15a [11], indicating the persisting challenge in powder manufacturing these types of feedstocks, consisting of materials with wide range of melting and freezing temperatures, with low deformability.

CSAM depositions of the RCCA (TaNbTiVCr) resulted in discontinuous deposits with poor interparticle bonding as shown in Fig. 16a. This behavior is consistent with the cold spray deposits manufactured using TaNbWTiVMoCr [11]. However, with minor additions (20 vol% in the feedstock) of relatively ductile material like Ti, that was inherently present in the RCCA composition, excellent buildability was observed, with good particle-particle bonding, which is evident from the magnitude of flattening of the RCCA particles. While the challenges with feedstock manufacturing still persist (Figs. 1, 2 and 15), the brittle nature of the RCCA feedstock has been countered with the addition of the ductile phase, without negotiating the mechanical response. The Ti particles imparted a cushioning effect upon the impacting RCCA particles that might have aided them in withstanding the shear stresses on the weaker grain boundaries inside the particle [43]. This effect also contributed to the closure of most defects, such as pores, which are

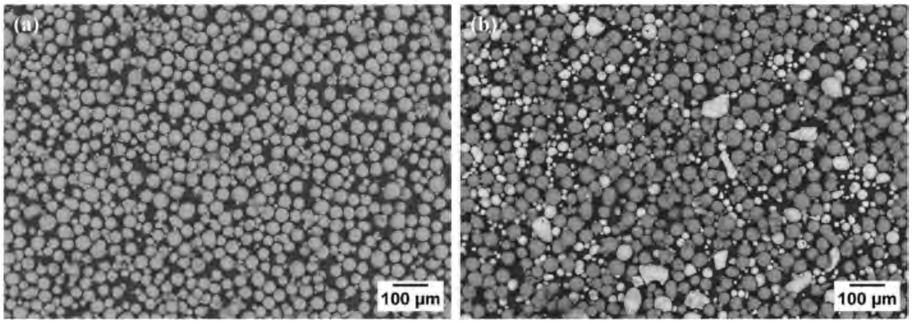

Fig. 8. SEM-BSE images of morphology of (a) CP-Ti (grade 1) (+20/-63 μm) (b) mixed feedstock (RCCA-40) used for LB-PBF processing.

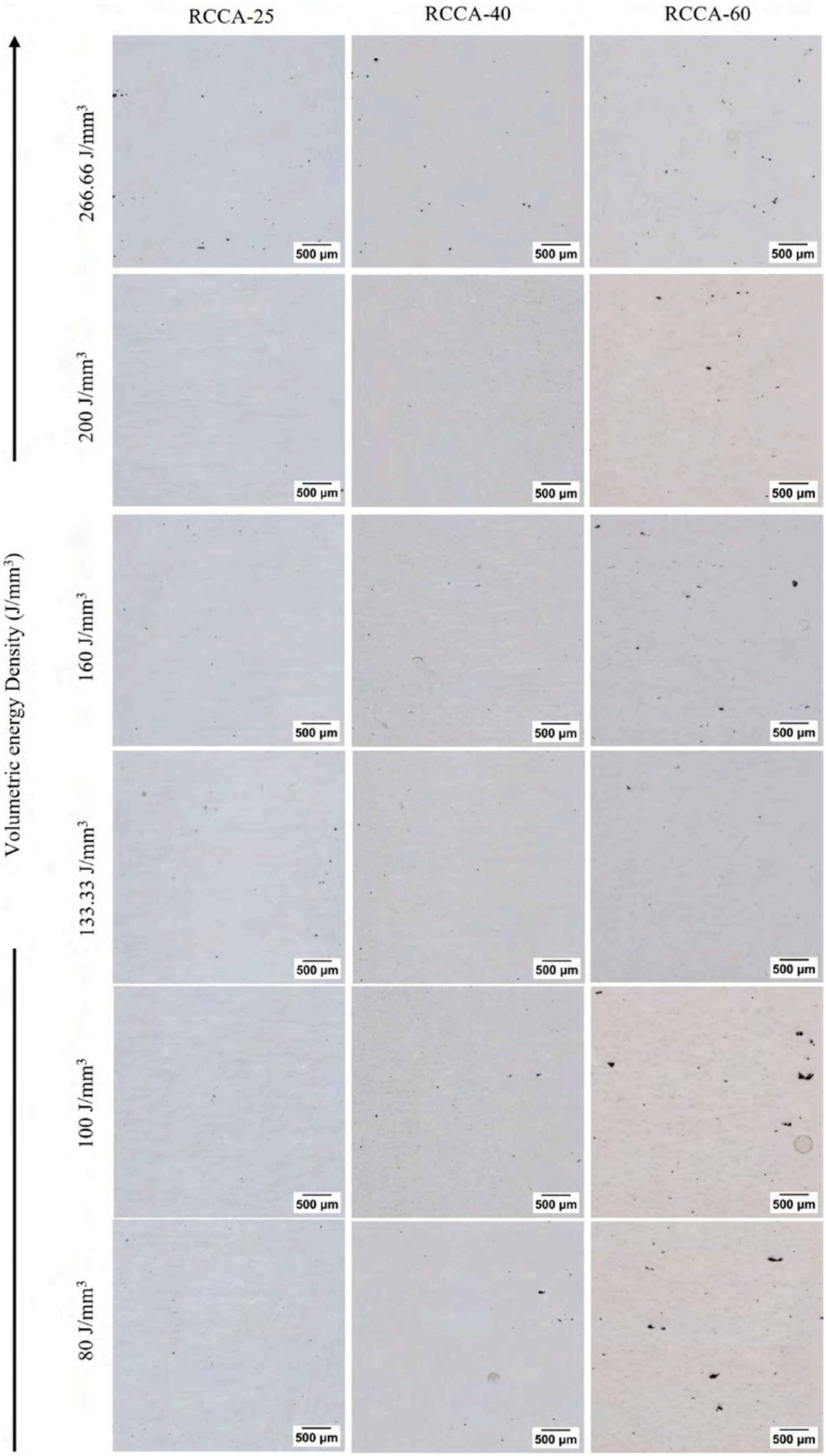

Fig. 9. OM images of cross sections of LB-PBF samples built using 180W laser power.

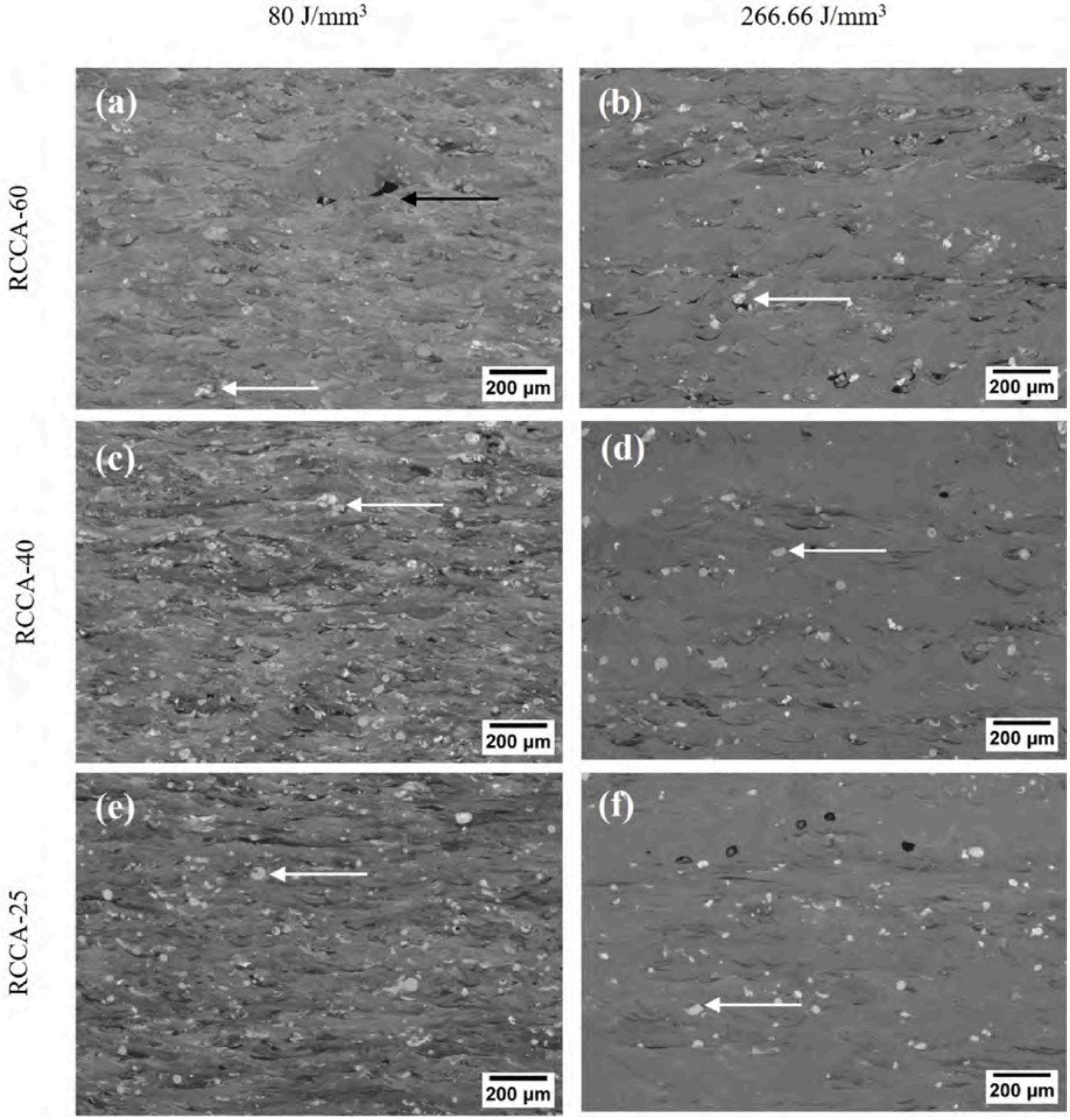

Fig. 10. SEM (BSE) images of RCCA + Ti mixtures processed with LB-PBF demonstrating the effect of VED on homogenization of microstructure at various volume fractions; black arrow shows the lack of fusion pores on the lower energy density specimen; white arrows show the unmolten Ta/Nb rich zones.

typically formed at the interfacial regions between the hard and soft phases within the deposits. Using pre-mixed feedstocks or adopting in-line powder mixing is expected to provide sufficient opportunity for individual RCCA particles to benefit from the ductility of the secondary phase, namely Ti. This, in turn, resulted in minimizing the interparticle interactions between the RCCA particles, thereby limiting the probability of particle fracture, as reported in the case of TaNbWTiVMoCr [11].

As observed in Fig. 16b, LB-PBF-processed RCCA exhibited a crack density of up to 2.8 mm/mm^2. Our previous study indicated that the use of feedstock with the inherent shortcomings resulted in defective specimens characterized by large crack networks, with crack densities up to 9 mm/mm^2, due to high magnitude of thermal residual stresses generated during processing, in the case of TaNbWTiVMoCr [11,44]. The formation of hot cracks was largely a result of shrinkage induced strains due to the restricted liquid feeding into the interdendritic regions during the solidification stage of printing [11,45,46]. Another notable limitation of the LB-PBF TaNbWTiVMoCr alloy was the formation of inhomogeneous microstructures from the feedstock powder. Although in current study, there was a reduction in crack density compared to the LB-PBF processed TaNbWTiVMoCr, the value still remains significantly high.

In this study, the first challenge, i.e. the minimization of crack formation, was achieved by the addition of Ti. Figs. 9–12 clearly shows this merit of Ti addition, which also suggests that there was a significant reduction in the thermal residual stresses, that were prevalent in the pure RCCA specimens (Fig. 16b) manufactured using LB-PBF. Although the melting and solidification cycles during LB-PBF processing promoted microstructural homogenization to an extent, complete homogenization was not achieved despite the addition of various volume fractions of Ti. This could be attributed to the use of relatively lower energy densities for printing selected to accommodate the presence of ductile Ti. Consequently, unmolten Ta/Nb rich areas were observed across in all the printed specimens (Figs. 10–14). While higher energy densities could enhance melting and mixing, they also might pose a risk of evaporation of Ti, which is necessary for the liquid supply to mitigate

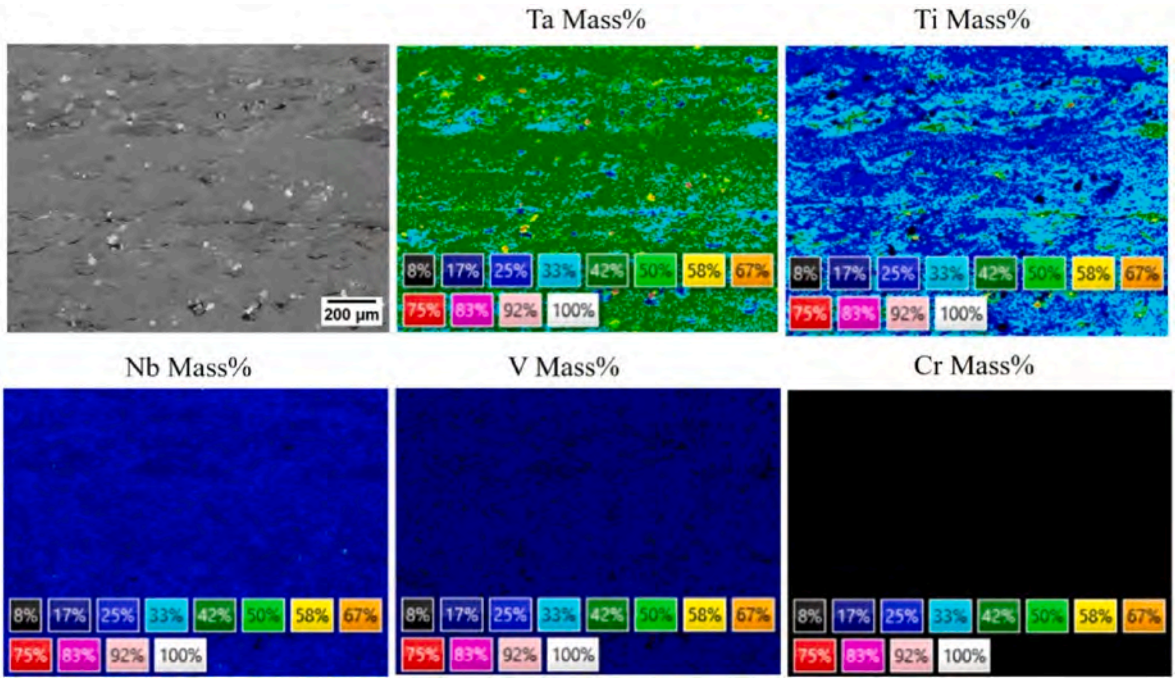

Fig. 11. EDS mapping of the cross section of RCCA-60 specimen LB-PBF printed at VED = 266.67 J/mm^3.

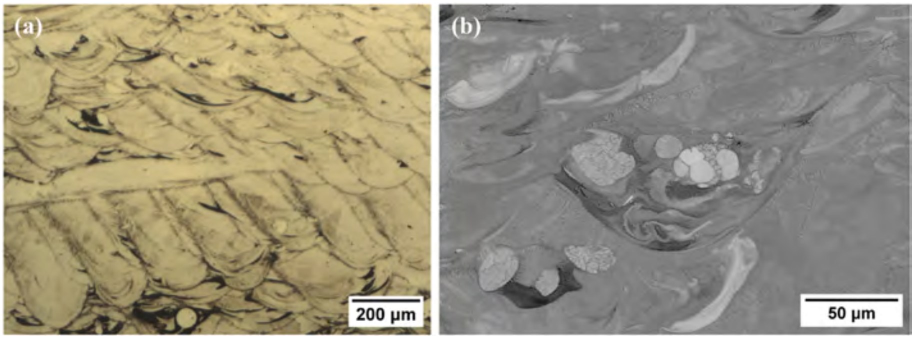

Fig. 12. (a) OM image of cross section (b) BSE – SEM image of melt pool indicating the filling action of Ti enveloping the unmolten Ta/Nb rich RCCA regions, in the RCCA-60 specimen built at VED = 266.66 J/mm^3.

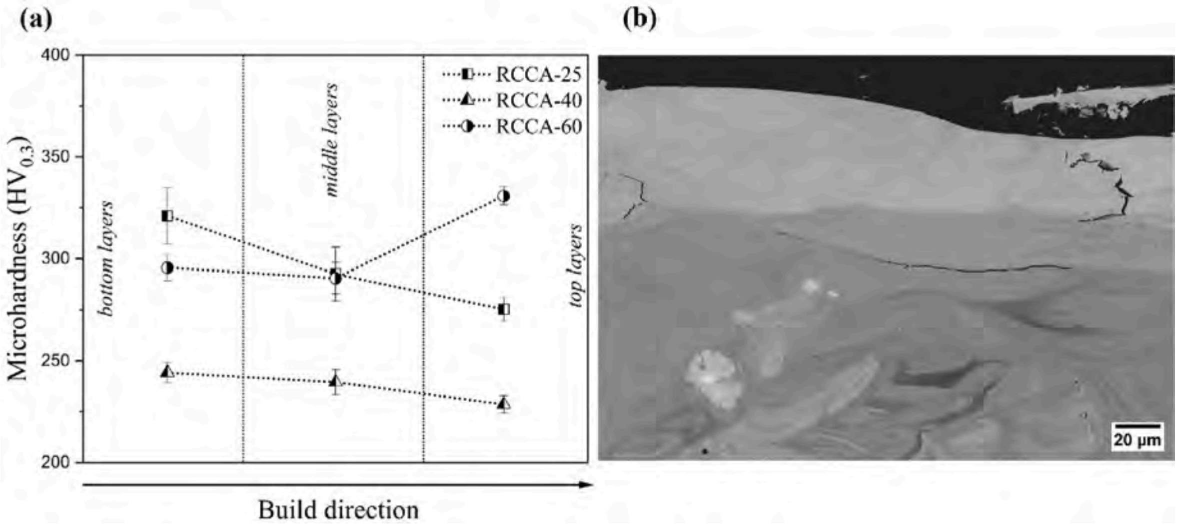

Fig. 13. (a) Microhardness variation of the LB-PBF printed RCCA specimens at VED = 266 J/mm^3; (b) Remelted layers on the RCCA-60 specimen.

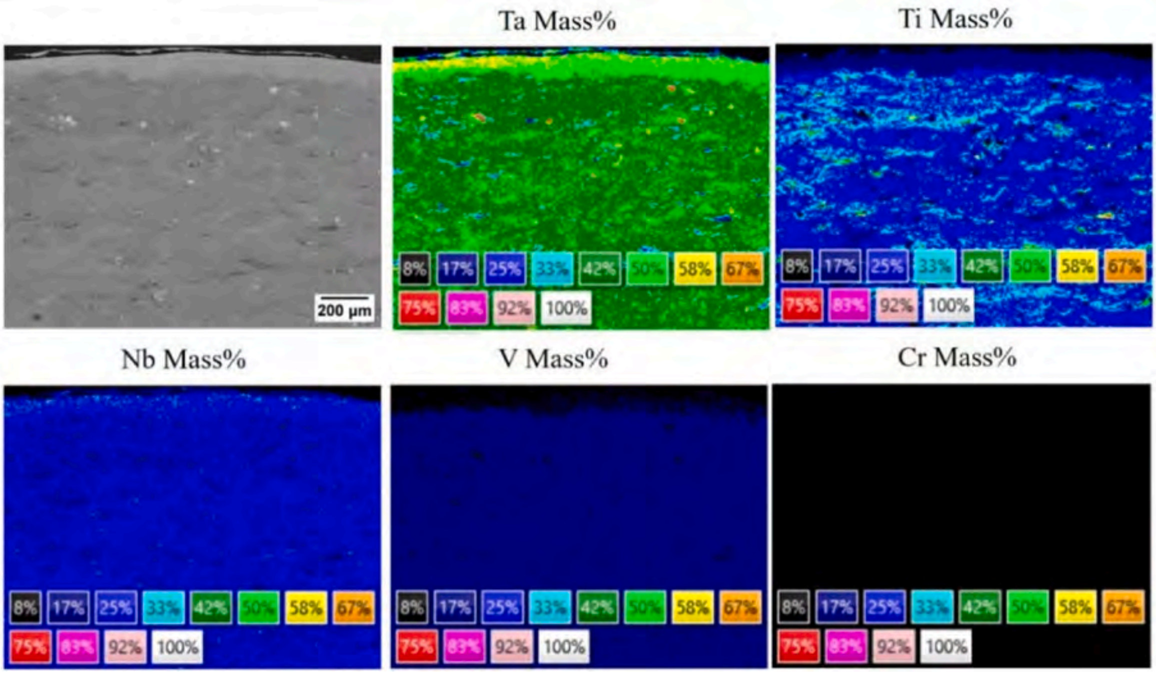

Fig. 14. EDS mapping of the cross section of RCCA-60 specimen LB-PBF printed at VED = 266 J/mm^3.

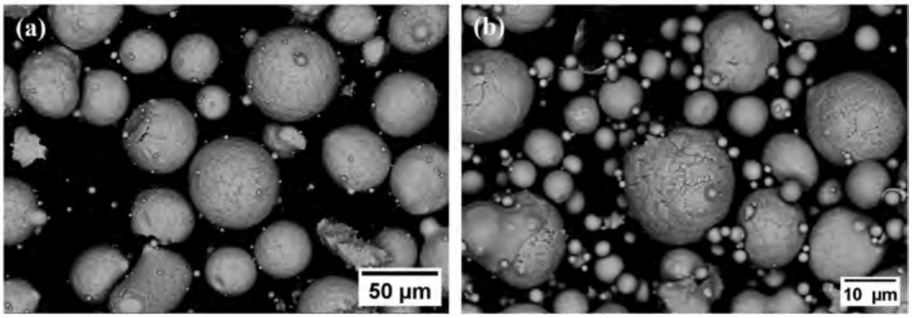

Fig. 15. Surface morphology of (a) TaNbWTiVMoCr particles [11] (b) RCCA used for current study (TaNbTiVCr).

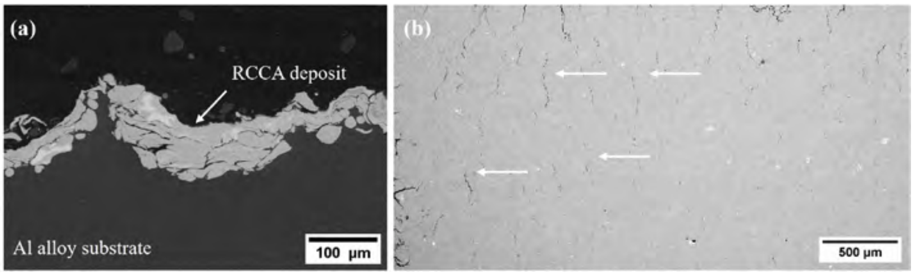

Fig. 16. (a) SEM-BSE image of CSAM deposition of RCCA showing discontinuous coating (b) SEM-BSE image of the LB-PBF printed RCCA specimen revealing the presence of cracks (white arrows).

hot cracks. As previously discussed in section 1, Xu et al. [25] studied the effect of addition of Ti to NbMoTaW during the LB-PBF processing. Results show that the presence of Ti in the mix enhanced the dispersion strengthening of the printed specimen by forming TiO2 precipitates, thereby improving its mechanical properties and reducing the entrapped interstitial oxygen content. Whilst the volume fraction of Ti addition can also be tailored to meet specific application demands, the microstructural analyses of the LB-PBF processed specimens demonstrate promising build qualities. A much better chemical and microstructural homogenization could be realized by repeated remelting, which, however, changed the composition and caused stress induced cracking.

Following strategies can be considered for achieving a better trade-off between chemical homogenization and the Ti evaporation. Optimized remelting scans [21,47], especially performed after each layer of printing at low energy densities has been reported to achieve better homogenization in terms of chemical composition and microstructure. Post-process heat treatments conducted at temperatures below the onset of Ti evaporation can promote solid-state diffusion of Ta and Nb, thereby reducing compositional heterogeneity originating from partially molten regions. Such approaches have been reported for Ti-based alloys and CCAs containing refractory elements, where extended annealing promotes chemical homogenization [48–51]. This could be modelled using Thermo-Calc and DICTRA software with relevant databases [52]. The approach should be balanced such that the as-built phase constitution is preserved, and excessive grain coarsening is avoided. While a systematic heat treatment study was beyond the scope of this work, this strategy offers a practical pathway to improve the chemical uniformity while preserving the Ti retention achieved under low energy density processing.

Overall, the CSAM deposits exhibited higher hardness than their LB-PBF counterparts at each mixing ratio. This difference can be attributed to the severe plastic deformation during particle impact in CSAM, where repeated effect of peening induces significant work hardening, which had resulted in much higher deposit hardness in the case of CSAM [38, 53–56].

Unlike CSAM deposits, microhardness measurements in LB-PBF specimens revealed a non-linear trend with respect to the volume fraction of RCCA in the powder bed. An initial decrease in microhardness was observed at RCCA-40, followed by a notable increase at RCCA-60 (Fig. 17a). The RCCA-60 specimens exhibited relatively high hardness values, ranging from 285 to 300 HV which can be attributed to the increased RCCA content in the printed specimens.

Despite the higher energy densities applied during processing, the microstructure of RCCA-60 specimens remained inhomogeneous (Fig. 10), suggesting incomplete mixing of the constituent elements during melting and solidification. Nevertheless, the formation of crack-free specimens at this composition was a promising outcome. It indicates that, although further improvements in homogeneity are necessary, the RCCA-60 composition demonstrated potential for application in mechanically demanding applications.

A reduction in the RCCA volume fraction to 40 % resulted in a measurable decrease in the hardness of the printed specimens. This reduction is primarily attributed to the increased presence of Ti, which exhibits lower intrinsic hardness compared to RCCA, particularly due to the formation of the α-Ti phase (as seen in Fig. 18). At this composition, even with increasing VED, the hardness further decreased, although the variation remained within a relatively narrow range (Fig. 17b). This suggests that the mechanical response at RCCA-40 is predominantly governed by the softer Ti-rich matrix, and the energy input has a limited influence on enhancing hardness at this RCCA content.

At lower RCCA concentrations, a sharp increase in the hardness of the printed specimens was observed (Fig. 17a). This enhancement is likely attributed to the formation of complex intermetallic or secondary phases, e.g. nitrides (i.e. Ti_2N) that may emerge when the Ti content in the matrix exceeds a certain threshold and reacts with residual nitrogen in the inert gas atmosphere. Nitrogen, since it cannot be filtered by the additional gas purification system mounted to the LB-PBF machine, is a residual gas during processing that is present in the low ppm regime and, thus, can get incorporated into the materials. XRD measurements carried out with the as-built samples indeed indicated the presence of low amounts of additional phases besides BCC and α-Ti. Due to the very small amounts of the secondary phases and the limiting detection limit of laboratory XRD an unambiguous characterization was not possible. However, there were indications for the presence of Ti_2N from the XRD plots. Reflections indicating the existence of this phase can be observed clearly in the RCCA-25 specimens built with 100 J/mm^2 (Fig. 18a). At this composition, the presence of Ti_2N precipitates may counterbalance the weakening by the α phase. Notably, the application of higher energy densities appears to facilitate this phenomenon (Fig. 18b), leading to a further increase in hardness (Fig. 17b). As a result, the hardness increased progressively, reaching a peak value of 305.51 HV at VED = 266.67 J/mm^3.

5. Conclusions

The refractory complex concentrated alloy (RCCA) TaNbTiVCr, typically posing critical challenges in additive manufacturing, were successfully processed with laser-based powder bed fusion and cold spray, by suitable additions of commercially pure Ti. Specific buildability aspects as well as microstructure and mechanical behavior, in terms of microhardness, were evaluated in both cases.

- Cold spray processing of the in-situ mixed RCCA-Ti feedstock resulted in good buildability, and minimal defects: 80 vol% of RCCA in the mixed feedstock yielded a deposit consisting of 61 vol% of RCCA, indicating a significant improvement compared to almost zero deposition efficiency of 100 vol% RCCA. The addition of Ti significantly enhanced RCCA deposition efficiency. Contrary to the attempts in depositing 100 vol% RCCA, the RCCA particles in the composite deposits were observed to have deformed as a result of continuous peening effect and had achieved sufficient particle flattening suggesting better build quality.
- Microhardness measurements on the cold spray deposits indicate that the average hardness of the deposit with the highest volume (61 vol%) of RCCA retained was approximately 410 HV, which is comparable with the result from the RCCA feedstock, despite the softer Ti addition. This suggests promising mechanical strength for structural applications.

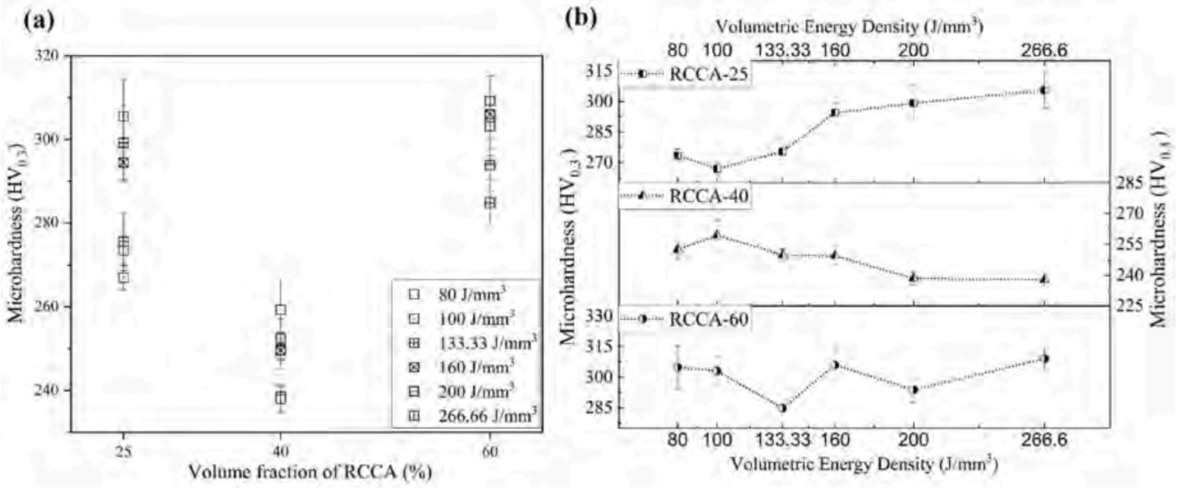

Fig. 17. Variation of microhardness in LB-PBF specimens with respect to the (a) VED and (b) volume fractions of mixing.

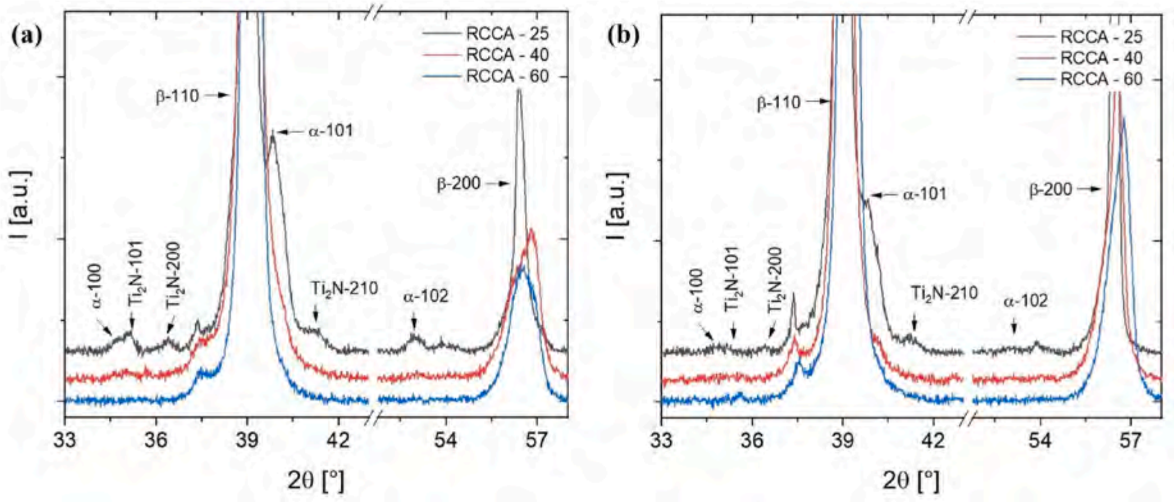

Fig. 18. XRD phase analyses of LB-PBF printed specimens printed with VED of (a) 100 J/mm^3 (b) 266 J/mm^3.

- Laser-based powder bed fusion of the RCCA-Ti mixtures indicated excellent build quality, compared to 100 vol% RCCA past trials. The mixtures increased relative densities exceeding in processing to 99.5 vol% regardless of the mixing compositions. Most specimens were devoid of solidification cracks likely due to the effective flow of molten liquid Ti during the later stages of solidification, which inhibited these cracks. However, the resulting microstructures exhibited regions with inhomogeneities from unmolten Ta/Nb due to the conservative processing conditions, which were chosen to avoid the risk of Ti evaporation.
- Microhardness measurements on laser-based powder bed fusion processed specimens revealed an irregular trend with respect to the volume fraction of RCCA in the feedstock: compositions of 60 vol% and 25 vol% volume of RCCA exhibited an average hardness in the range of 280–310 HV, whereas the specimen with 40 vol% RCCA showed a significantly lower mean hardness of approximately 240 HV. Domination of α-Ti phase at this composition, and the formation of hard phases such as titanium nitrides at the higher Ti concentrations could have attributed to this variation.

This study provides a viable approach for processing RCCA in composite feedstock format using additive manufacturing methods like cold spray and laser-based powder bed fusion. While the results show significant promise in terms of build quality and mechanical performance compared with trials using 100 % RCCA, the need for post-processing remains critical. In the case of laser-based powder bed fusion, this can enhance elemental mixing and promote homogenization. On the other hand, suitable post-processing is to be explored further to facilitate metallurgical bonding between the constituent particles in the case of cold spray. Future research can expand the potential applications, by leveraging the merits of the two additive manufacturing techniques in design and fabrication of functionally graded parts.

CRediT authorship contribution statement

Magesh Kumaravel: Writing – original draft, Visualization, Validation, Investigation, Formal analysis. **Joachim Gussone:** Writing – original draft, Visualization, Validation, Methodology, Investigation, Formal analysis. **Meaghi Sikder:** Writing – original draft, Visualization, Validation. **Amir Ardeshiri Lordejani:** Writing – review & editing, Methodology, Investigation. **Ida S. Berglund:** Writing – review & editing, Supervision. **Jan Haubrich:** Writing – review & editing, Methodology, Formal analysis. **Sara Bagherifard:** Writing – review & editing, Supervision, Methodology, Conceptualization. **Mario Guagliano:** Writing – review & editing, Supervision, Resources, Project administration, Methodology.

Declaration of competing interest

The authors declare that they have no known competing financial interests or personal relationships that could have appeared to influence the work reported in this paper.

Acknowledgement

The research leading to these results has received funding from the European Union's Horizon 2020 programme for research and innovation under grant agreement no. 101004172 (ATLAS, Advanced Design of High Entropy Alloys Based Materials for Space Propulsion).

Data availability

Data will be made available on request.

References

[1] D.B. Miracle, O.N. Senkov, A critical review of high entropy alloys and related concepts, Acta Mater. 122 (2017) 448–511.
[2] S.K. Dewangan, A. Mangish, S. Kumar, A. Sharma, B. Ahn, V. Kumar, A review on high-temperature applicability: a milestone for high entropy alloys *engineering science and technology, an international journal* 35 (2022).
[3] N. Kaushik, A. Meena, H.S. Mali, High entropy alloy synthesis, characterisation, manufacturing & potential applications: a review, Mater. Manuf. Proc. 37 (2022) 1085–1109.
[4] O.N. Senkov, D.B. Miracle, K.J. Chaput, J.P. Couzinie, Development and exploration of refractory high entropy alloys - a review, J. Mater. Res. 33 (2018) 3092–3128.
[5] A. Meghwal, A. Anupam, B.S. Murty, C.C. Berndt, R.S. Kottada, A.S.M. Ang, Thermal spray high-entropy alloy coatings: a review, J. Therm. Spray Technol. 29 (2020) 857–893.
[6] M. Kumaravel, S. Bagherifard, M. Guagliano, Advancements in deposition of high entropy alloys using cold spray technology, J. Therm. Spray Technol. 34 (2024) 1–36.
[7] A. Ostovari Moghaddam, N.A. Shaburova, M.N. Samodurova, A. Abdollahzadeh, E. A. Trofimov, Additive manufacturing of high entropy alloys: a practical review, J. Mater. Sci. Technol. 77 (2021) 131–162.
[8] M.R. Abdullah, Z. Peng, “Review and perspective on additive manufacturing of refractory high entropy alloys”, Mater. Today Adv. 22 (2024).
[9] B. Vrancken, R.K. Ganeriwala, M.J. Matthews, Analysis of laser-induced microcracking in tungsten under additive manufacturing conditions: experiment and simulation, Acta Mater. 194 (2020) 464–472.
[10] A.V. Müller, G. Schlick, R. Neu, C. Anstätt, T. Klimkait, J. Lee, B. Pascher, M. Schmitt, C. Seidel, Additive manufacturing of pure tungsten by means of selective laser beam melting with substrate preheating temperatures up to 1000 ∘ C, Nucl. Mater. Energy 19 (2019) 184–188.
[11] M. Kumaravel, Y. Eynolghozzat, J. Gussone, F. Yan, A.A. Lordejani, J. Haubrich, G. Requena, I.S. Berglund, M. Guagliano, S. Bagherifard, Elucidating the challenges

in the development and deployment of refractory complex concentrated alloys for additive manufacturing, Addit. Manuf. (2024) 104286.
[12] W. Li, H. Assadi, F. Gaertner, S. Yin, A review of advanced composite and nanostructured coatings by solid-state cold spraying process, Crit. Rev. Solid State Mater. Sci. 44 (2019) 109–156.
[13] R.A. Wicaksono, A. Ardeshiri Lordejani, S. Bagherifard, Current trends and future perspective for cold spray metal-ceramic composites, Adv. Eng. Mater. 27 (2025).
[14] F. Zarei, A. Ardeshiri Lordejani, S. Ruan, S. Yin, M. Guagliano, R. Lupoi, S. Bagherifard, Evaluating the application of cold spray technology for the deposition of copper–graphene composite coatings, Coatings 15 (2025).
[15] Y. Zou, Z. Qiu, C. Huang, D. Zeng, R. Lupoi, N. Zhang, S. Yin, Microstructure and tribological properties of Al2O3 reinforced FeCoNiCrMn high entropy alloy composite coatings by cold spray, Surf. Coat. Technol. 434 (2022).
[16] P. Han, W. Wang, Z. Liu, T. Zhang, Q. Liu, X. Guan, K. Qiao, D. Ye, J. Cai, Y. Xie, K. Wang, Modification of cold-sprayed high-entropy alloy particles reinforced aluminum matrix composites via friction stir processing, J. Alloys Compd. 907 (2022).
[17] X. Fan, X. Chu, Y. Xie, D. Zhou, Q. Tian, Y. Tong, P.K. Liaw, S. Chen, F. Meng, Microstructure and mechanical properties of cold spray additive manufactured and post heat treated high-entropy alloys with mixed CoCrFeNi and Ti powders, J. Mater. Res. Technol. 27 (2023) 4328–4344.
[18] B. Vrancken, L. Thijs, J.P. Kruth, J. Van Humbeeck, Microstructure and mechanical properties of a novel β titanium metallic composite by selective laser melting, Acta Mater. 68 (2014) 150–158.
[19] E.G. Brodie, A.E. Medvedev, J.E. Frith, M.S. Dargusch, H.L. Fraser, A. Molotnikov, Remelt processing and microstructure of selective laser melted Ti25Ta, J. Alloys Compd. 820 (2020).
[20] E.G. Brodie, J. Richter, T. Wegener, T. Niendorf, A. Molotnikov, Low-cycle fatigue performance of remelted laser powder bed fusion (L-PBF) biomedical Ti25Ta, Mater. Sci. Eng., A 798 (2020).
[21] H. Li, E.G. Brodie, C. Hutchinson, Predicting the chemical homogeneity in laser powder bed fusion (LPBF) of mixed powders after remelting, Addit. Manuf. 65 (2023).
[22] P. Qin, L.Y. Chen, C.H. Zhao, Y.J. Liu, C.D. Cao, H. Sun, L.C. Zhang, Corrosion behavior and mechanism of selective laser melted Ti35Nb alloy produced using pre-alloyed and mixed powder in Hank's solution, Corros. Sci. 189 (2021).
[23] J.C. Wang, Y.J. Liu, P. Qin, S.X. Liang, T.B. Sercombe, L.C. Zhang, Selective laser melting of Ti–35Nb composite from elemental powder mixture: microstructure, mechanical behavior and corrosion behavior, Mater. Sci. Eng., A 760 (2019) 214–224.
[24] F. Huber, D. Bartels, M. Schmidt, In situ alloy formation of a wmotanbv refractory metal high entropy alloy by laser powder bed fusion (Pbf-lb/m), Materials 14 (2021).
[25] J. Xu, M. Qin, S. Du, P. Kumar, J. Zhu, Y. Jia, Z. Yan, Y. Xie, P. Dong, K. Feng, Z. Li, Q. Zhou, X. Liang, U. Ramamurty, Enhancing the strength and plasticity of laser powder bed fused NbMoTaW refractory high-entropy alloy via Ti alloying, J. Alloys Compd. 1001 (2024).
[26] Z.D. Han, N. Chen, S.F. Zhao, L.W. Fan, G.N. Yang, Y. Shao, K.F. Yao, Effect of Ti additions on mechanical properties of NbMoTaW and VNbMoTaW refractory high entropy alloys, Intermetallics (Barking) 84 (2017) 153–157.
[27] B.E. Carroll, R.A. Otis, J.P. Borgonia, J.O. Suh, R.P. Dillon, A.A. Shapiro, D. C. Hofmann, Z.K. Liu, A.M. Beese, Functionally graded material of 304L stainless steel and inconel 625 fabricated by directed energy deposition: characterization and thermodynamic modeling, Acta Mater. 108 (2016) 46–54.
[28] A. Reichardt, R.P. Dillon, J.P. Borgonia, A.A. Shapiro, B.W. McEnerney, T. Momose, P. Hosemann, Development and characterization of Ti-6Al-4V to 304L stainless steel gradient components fabricated with laser deposition additive manufacturing, Mater. Des. 104 (2016) 404–413.
[29] H. Sahasrabudhe, R. Harrison, C. Carpenter, A. Bandyopadhyay, Stainless steel to titanium bimetallic structure using LENSTM, Addit. Manuf. 5 (2015) 1–8.
[30] A.A. Tiamiyu, C.A. Schuh, Particle flattening during cold spray: mechanistic regimes revealed by single particle impact tests, Surf. Coat. Technol. 403 (2020).
[31] M.R. Rokni, S.R. Nutt, C.A. Widener, V.K. Champagne, R.H. Hrabe, Review of relationship between particle deformation, coating microstructure, and properties in high-pressure cold spray, J. Therm. Spray Technol. 26 (2017) 1308–1355.
[32] R. Huang, H. Fukanuma, Study of the influence of particle velocity on adhesive strength of cold spray deposits, J. Therm. Spray Technol. 21 (2012) 541–549.
[33] D. Goldbaum, R.R. Chromik, N. Brodusch, R. Gauvin, Microstructure and mechanical properties of Ti cold-spray splats determined by electron channeling contrast imaging and nanoindentation mapping, Microsc. Microanal. 21 (2015) 570–581.
[34] G. Sundararajan, N.M. Chavan, G. Sivakumar, P. Sudharshan Phani, Evaluation of parameters for assessment of inter-splat bond strength in cold-sprayed coatings, J. Therm. Spray Technol. 19 (2010) 1255–1266.
[35] W. Li, C. Cao, S. Yin, Solid-state cold spraying of Ti and its alloys: a literature review, Prog. Mater. Sci. 110 (2020).
[36] W. Wong, A. Rezaeian, E. Irissou, J.G. Legoux, S. Yue, Cold Spray Characteristics of Commercially Pure Ti and Ti-6Al-4V *THERMEC 2009 Supplement* Advanced Materials Research, 89, Trans Tech Publications Ltd, 2010, pp. 639–644.
[37] W. Wong, E. Irissou, A.N. Ryabinin, J.G. Legoux, S. Yue, Influence of helium and nitrogen gases on the properties of cold gas dynamic sprayed pure titanium coatings, J. Therm. Spray Technol. 20 (2011) 213–226.
[38] P. Cavaliere, A. Perrone, A. Silvello, A. Laska, G. Blasi, I.G. Cano, B. Sadeghi, S. Nagy, Cyclic behavior of FeCoCrNiMn high entropy alloy coatings produced through cold spray, J. Alloys Compd. 931 (2023).
[39] L. Liu, D. Wang, C. Han, Y. Li, T. Wang, Y. Wei, W. Zhou, M. Yan, Y. Liu, S. Wei, Y. Yang, Additive manufacturing of multi-materials with interfacial component gradient by in-situ powder mixing and laser powder bed fusion, J. Alloys Compd. 978 (2024).
[40] H. Fredriksson, K. Hansson, A. Olsson, On the mechanism of liquid copper penetration into iron grain boundaries, Scand. J. Metall. 30 (2001) 41–50.
[41] T. DebRoy, H.L. Wei, J.S. Zuback, T. Mukherjee, J.W. Elmer, J.O. Milewski, A. M. Beese, A. Wilson-Heid, A. De, W. Zhang, Additive manufacturing of metallic components – process, structure and properties, Prog. Mater. Sci. 92 (2018) 112–224.
[42] R. Jiang, A. Mostafaei, Z. Wu, A. Choi, P.W. Guan, M. Chmielus, A.D. Rollett, Effect of heat treatment on microstructural evolution and hardness homogeneity in laser powder bed fusion of alloy 718, Addit. Manuf. 35 (2020).
[43] C. Huang, W. Li, M.P. Planche, H. Liao, G. Montavon, In-situ formation of Ni-Al intermetallics-coated graphite/Al composite in a cold-sprayed coating and its high temperature tribological behaviors, J. Mater. Sci. Technol. 33 (2017) 507–515.
[44] N.C. Levkulich, S.L. Semiatin, J.E. Gockel, J.R. Middendorf, A.T. DeWald, N. W. Klingbeil, The effect of process parameters on residual stress evolution and distortion in the laser powder bed fusion of Ti-6Al-4V, Addit. Manuf. 28 (2019) 475–484.
[45] M. Rappaz, J.-M. Drezet, M. Gremaud, A new hot-tearing criterion 30 (1999).
[46] D.G. Eskin, Suyitno, L. Katgerman, Mechanical properties in the semi-solid state and hot tearing of aluminium alloys, Prog. Mater. Sci. 49 (2004) 629–711.
[47] A. Chouhan, M. Hesselmann, A. Toenjes, L. Mädler, N. Ellendt, Numerical modelling of in-situ alloying of Al and Cu using the laser powder bed fusion process: a study on the effect of energy density and remelting on deposited track homogeneity, Addit. Manuf. 59 (2022).
[48] D. Vogiatzief, A. Evirgen, S. Gein, V.R. Molina, A. Weisheit, M. Pedersen, Laser powder bed fusion and heat treatment of an AlCrFe2Ni2 high entropy alloy, Front. Mater. 7 (2020).
[49] Guo S and Liu C T Phase Stability in High Entropy Alloys: Formation of solid-solution Phase or Amorphous Phase].
[50] K. An, T. Yang, J. Feng, H. Deng, X. Zhang, Z. Zhao, Q. Meng, J. Qi, F. Wei, Y. Sui, Influence of Al and Ti alloying and annealing on the microstructure and compressive properties of cr-fe-ni multi-principal element alloy, Metals 14 (2024).
[51] Y. Li, J. Xie, Z. Zhang, X. Zhang, X. Ren, L. Chen, Effect of homogenization annealing on microstructure and mechanical properties of AlMo0.5NbTa0.5TiZr refractory high entropy alloy manufactured by laser metal deposition, Mater. Char. 225 (2025).
[52] J.-O. Anderson, Thomas Helander, Lars Höglund, Pingfang Shi, Bo Sundman, Thermo-Calc & DICTRA, Comput. Tool Mater. Sci. Calphad 26 (2002) 273–312.
[53] H. Assadi, T. Schmidt, H. Richter, J.O. Kliemann, K. Binder, F. Gärtner, T. Klassen, H. Kreye, On parameter selection in cold spraying, J. Therm. Spray Technol. 20 (2011) 1161–1176.
[54] A.W.Y. Tan, W. Sun, A. Bhowmik, J.Y. Lek, I. Marinescu, F. Li, N.W. Khun, Z. Dong, E. Liu, Effect of coating thickness on microstructure, mechanical properties and fracture behaviour of cold sprayed Ti6Al4V coatings on Ti6Al4V substrates, Surf. Coat. Technol. 349 (2018) 303–317.
[55] T.H. Van Steenkiste, J.R. Smith, R.E. Teets, Aluminum Coatings via Kinetic Spray with Relatively Large Powder Particles, 154, 2002.
[56] R.F. Vaz, A. Garfias, V. Albaladejo, J. Sanchez, I.G. Cano, How increasing cold spray coatings thickness affects their residual stress and properties, Surf. Coat. Technol. 485 (2024).